Supplementary Information for

Phase-Multiplied Interferometry via Cavity Dynamics for Resolution-Enhanced Coherent Ranging

Yifan Wang[1], Jinsong Liu[1], Chenxiao Lin[1], Xin Xu[1], Yu Wang[1], Xinhang Yang[1], Binbin Xie[1], Jibo Han[2], Tengfei Wu[2], Xuling Lin[3], Liangcai Cao[1], Hongbo Sun[1], Yidong Tan[1]

Correspondence: Yidong Tan (Tanyd@tsinghua.edu.cn)

[1]State Key Laboratory of Precision Measurement Technology and Instruments, Department of Precision Instruments, Tsinghua University, Beijing 100084, China

[2]National Key Laboratory of Metrology and Calibration, Beijing Changcheng Institute of Metrology & Measurement, Beijing 100095, China

[3]Beijing Institute of Space Mechanics and Electricity, Beijing 100094, China

These authors contributed equally: Yifan Wang, Jinsong Liu, and Chenxiao Lin

1 Optical spectrum analysis with laser feedback

With laser feedback, the output spectrum of the laser exhibits sidebands, as analyzed by Eq. (4) in the main text. Since the modulation frequency in this study is at the MHz level, which is significantly lower than the resolution of the typical optical spectrum analyzer and scanning Fabry-Perot interferometer. Thus, it is not feasible to use conventional instruments to directly observe these sidebands[1]. To address this limitation, we construct an optical setup as shown in Fig. S1, which combines part of the output from the fiber laser with a tunable laser source (TLS) and detects the beat between them. The signal power spectrum is then analyzed using an electronic spectrum analyzer (ESA). The TLS used in this experiment possesses a linewidth better than 200 kHz, and its wavelength setting resolution is 0.1 pm, which allows it to match the fiber laser and ensures that the beat frequency signal falls within the detection range of the photodetector (PD). The fiber laser operates under thermal and vibration isolation conditions, and its output is frequency-shifted by an acousto-optic modulator (AOM) before returning to the laser cavity. Considering the linewidths of both light sources, the AOM modulation frequency is set to 1 MHz to distinguish the sidebands better. Additionally, an optical isolator (ISO) is used to eliminate the influence of the TLS on the fiber laser. We record the power spectra in the presence of frequency shift feedback and under free-running conditions, as shown in Fig. 2(c) in the main text.

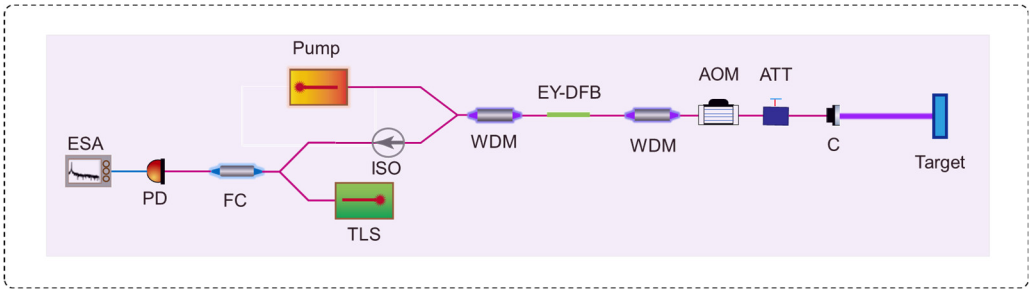

Fig. S1 Schematic diagram of fine spectrum analysis. EY-DFB, erbium-ytterbium co-doped distributed feedback laser. AOM, acousto-optic modulator. WDM, wavelength division multiplexer. ISO, optical isolator. PD, photodetector. ATT, adjustable attenuator. C, collimator. FC, fiber coupler. TLS, tunable laser source. ESA, electronic spectrum analyzer.

2 Signal generation and acquisition

Fig. S2 illustrates the signal generation and acquisition layout. A symmetric ramp signal generated by an arbitrary waveform generator (AWG) is amplified by a power amplifier (PA) to drive the piezoelectric ceramic actuator (PZT). Synchronization between data acquisition and galvanometer motion is ensured by a TTL trigger signal output simultaneously with the ramp signal from the AWG. Signals from PD (corresponding to the laser output) and balanced photodetector (BPD, representing the auxiliary interferometer output) are recorded concurrently using a data acquisition card (DAQ). As theoretically predicted, the laser output contains the target beat signal for measurement, while the auxiliary signal exhibits matching frequency components. To isolate these components, a high-pass filter is employed, leveraging the typical excess length of the delay fiber relative to the target distance. The two galvanometers, controlled individually by a dual-channel galvanometer controller, remain stationary during data acquisition. Finally, recorded signals are analyzed computationally. Signal-to-noise ratio (SNR) analysis of the fundamental beat signal yields an error signal, which is output to an analog output device (AOD) for controlling the semiconductor optical amplifier (SOA) in adaptive intensity compensation.

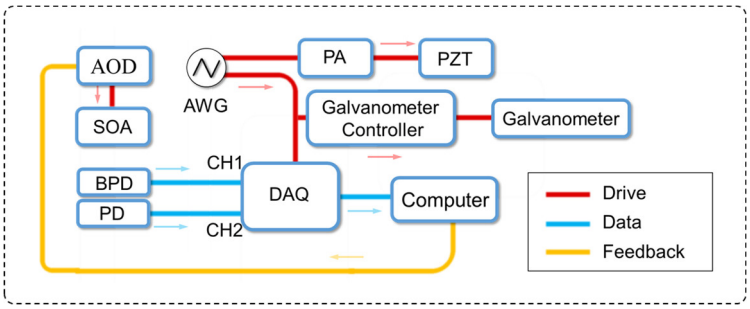

Fig. S2 Schematic diagram of signal generation and acquisition. AWG, arbitrary waveform generator. DAQ, data acquisition card. PZT, piezoelectric ceramic actuator. PA, power amplifier. PD, photodetector. BPD, balanced photodetector. AOD, analog output device. SOA, semiconductor optical amplifier. The red, blue, and yellow lines represent the drive signals, data signals, and feedback control signals.

3 Performance of adaptive intensity compensation

Higher-order harmonics demonstrate significant sensitivity to optical feedback strength, limiting their applicability in large-dynamic-range measurement scenarios such as scattering target imaging. To address this, we implement an adaptive compensation scheme using optical circulators and SOA in the configuration illustrated in Fig. S3a. We first calculate the SNR of the fundamental signal, using a 60 dB threshold, and then dynamically adjust the drive current to regulate probe light intensity, thereby stabilizing feedback strengths. During experiments, this current modulation can prevent system instability or signal loss.

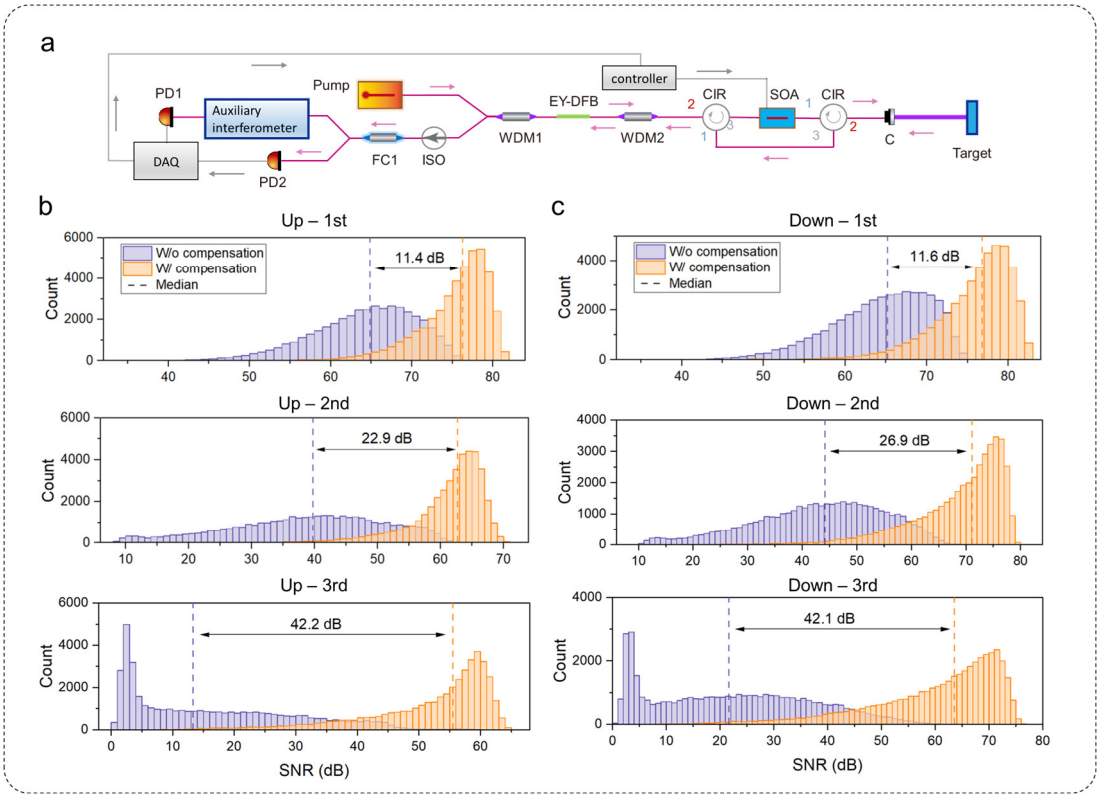

Fig. S3 Adaptive intensity compensation device. a Schematic diagram of the experimental setup. The controller connects the external modulation port of the SOA, and the gain or loss factor is determined by the output voltage. CIR, circulator. **b** The histogram of SNR for harmonics from 1st to 3rd in upward scanning before and after compensation. The data originates from 3D-imaging results in Fig. 4b. The purple and orange dashed lines denote the median SNR with and without compensation. **c** The histogram of SNR for harmonics from the 1st to 3rd in downward scanning.

Fig. S3b compares the SNR of harmonic signals from 1st to 3rd before and after compensation in 3D imaging experiments, with median values of SNR representing the intensity response. The 3rd harmonic exhibits over 42dB enhancement with compensation. Notably, measurements with SNR less than 10 dB may induce excessive errors and low

reliability. Without compensation, 41% of the 3rd data points fall below this threshold, reducing to 1% after compensation. Additionally, slight SNR discrepancies between upward and downward scans under identical conditions are observed, primarily attributable to polarization matching variations.

4 Comparison with the Conventional FMCW Ranging System

Comparison experiments are conducted to evaluate the enhancement in SNR for both harmonic generation and the fundamental interference signal induced by laser feedback. The experimental setups for the two systems, conventional FMCW and LFPM ranging system, are shown in Fig. S4. Identical experimental conditions are maintained, including laser output power, target distance and orientation, and beam divergence angle, with all components shared except some devices marked in the figure. In the conventional system, an optical circulator, CIR1, is used for transmitting and collecting the measurement beam, and two fiber couplers, FC2 and FC3, generate the interference signal. The power emitted from the collimator is 41 μW, and photodetector PD2 receives 24 μW of the combined beam. In contrast, for the LFPM system, interference occurs intrinsically within the laser cavity, eliminating the external reference arm. Consequently, the output beam is directed onto the target, and the interference signal is acquired by directly monitoring the laser output. An adjustable optical attenuator, ATT1, is employed to adjust the measurement beam power to 21 μW, approximately half that of the conventional system, ensuring comparable intensity at the detector. Additionally, another attenuator, ATT2, is used to control the power incident on the detector, matching the level at PD2. The comparison results are detailed in the main text.

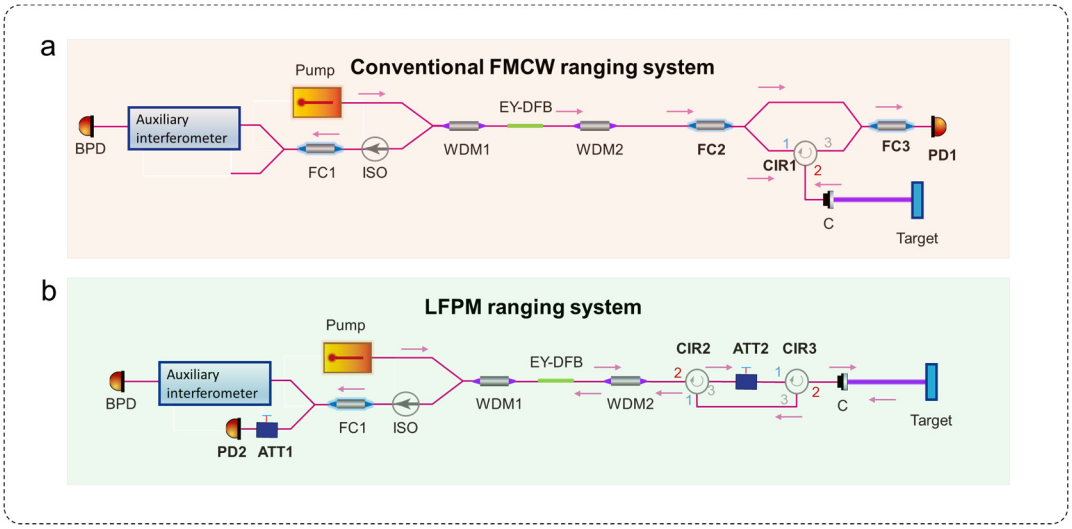

Fig. S4 Schematics of experimental setups. a Conventional FMCW ranging system. **b** Proposed LFPM ranging system. All components are shared except those highlighted in bold.

5 Ranging results with CZT

We further evaluate the precision of distance measurements derived from these harmonics. In contrast to the tests in Fig. 3, data analysis in this part employs the chirp-Z transform (CZT) for spectral interpolation. It is worth noting that while CZT or zero-padding interpolation can improve the data resolution to facilitate the extraction of the peak frequency of the signal, they cannot reduce the spectral bandwidth of the signal[2]. In the experiment, an optical fiber mirror is used as the target, located approximately 3.13 m from the light source. The output power of the laser source is 2 mW, with a maximum sweep bandwidth of 110 GHz. We use CZT to enhance the spectral interval to 0.1 μm. The measurement results are shown in Fig. S5a, where the inset displays the detailed spectra of the 1st and 13th harmonics. Across 10 repeated measurements, the standard deviations of the 9th-order and lower harmonics are close to each other and remain below 3 μm.

The linearity test of the system is also carried out, which demonstrates the nonlinear error in measurements. The precision of the stage is 50 nm, which can be taken as the standard. An aluminum sheet works as a target, which is driven by the stage with 10 cm, covering the whole travel range of the stage. The acquired data, linear fitting, and residual error are marked in Fig. S5b. The maximum residual error is 43 μm from the 4th harmonics, corresponding to 4.3×10^{-4} linearity within 10 cm.

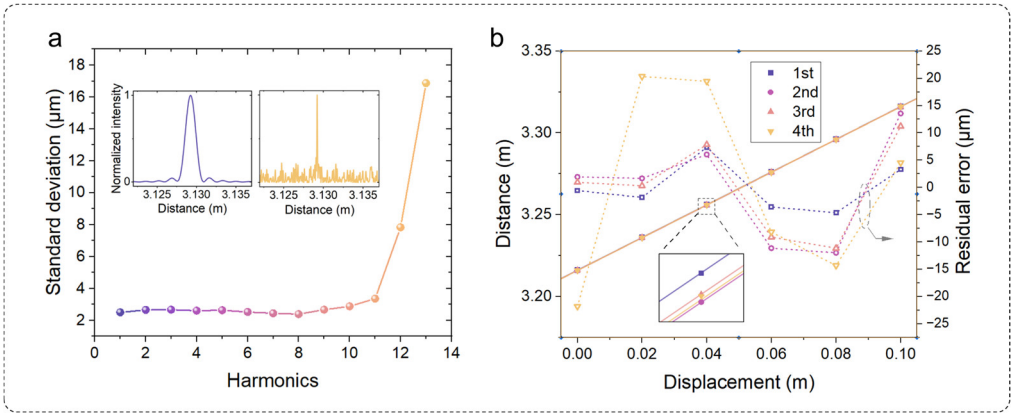

Fig. S5 Ranging results of harmonics using CZT. a Precision test of harmonics. We employ a reflector as the target, and repeat 10 measurements. The standard deviations of the 1st to 13th harmonics are shown. The insets show the local spectra of the 1st and the 13th with normalized intensity. Their FWHM exhibits a distinct difference. **b** Linearity test of harmonics. Solid lines denote the linear-fitting results, and dashed lines represent the residual error of ranging employing the 1st to 4th harmonics. The inset shows the details of the data at 0.04 m.

6 Solutions to the operating frequency equation

The evolution of the laser frequency in a ranging system, under the influence of frequency-shift feedback, is governed by Eq. (4) in the main text[3]. This equation can be analyzed graphically by defining the left-hand side as $f_1(\omega)$ and the right-hand side as $f_2(\omega)$, and plotting them in the same coordinate system.

$$\begin{aligned} f_1(\omega) &= \omega(t) - \omega_c \\ f_2(\omega) &= \kappa\gamma_c \sin[\Omega t - \omega(t)\tau] \end{aligned} \tag{S1}$$

As shown in Fig. S6a, the two curves intersect at least once. The solutions depends on the feedback strength, κ, and can be categorized into three regimes: 1) $\kappa\gamma_c\tau < 1$, the magnitude of the derivative $|f_2'(\omega)|$ is less than 1, and the equation has only one solution, corresponding to single-mode operation of the laser; 2) $\kappa\gamma_c\tau = 1$, the critical condition of single-mode operation; 3) $\kappa\gamma_c\tau > 1$, multiple modes are excited, leading to mode hopping within the laser resonator. Notably, all experimental investigations in this study are conducted under single-mode operation to ensure the validity of the measurements.

Additionally, the frequency difference Ω between the feedback light and the intracavity light introduces a time-varying phase shift, even if the feedback strength remains constant over time. Fig. S6b illustrates the curves under different phase shifts, showing that the actual output frequency of the laser will oscillate periodically within a certain range, with the size of this range proportional to the feedback strength.

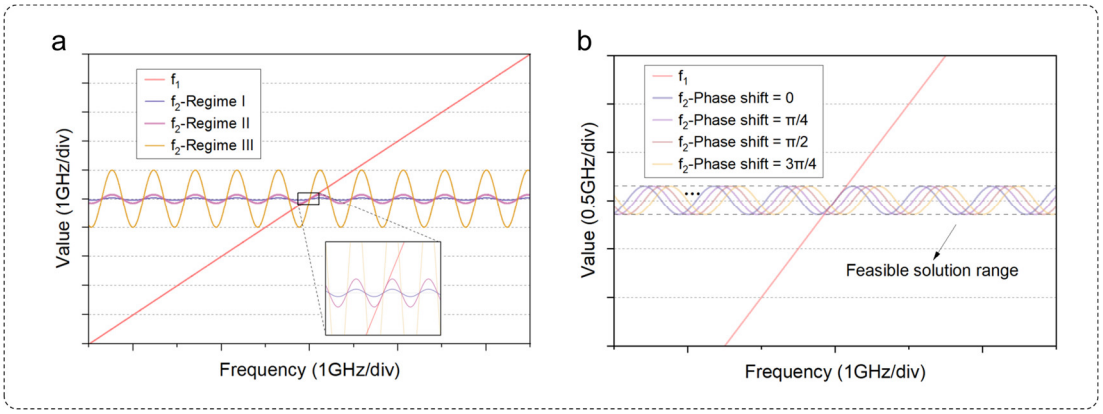

Fig. S6 Schematic diagram of solutions to the operating frequency equation. a Define two functions, f_1 and f_2, representing the expression of the equation, and their intersections denote the solution. The inset shows the details of the intersection. According to the feedback strength, the solution can be classified in three regimes, corresponding to $\kappa\gamma_c\tau$ 1) less than, 2) equal to, or 3) larger than 1. **b** Solutions of the equation with various phase shifts in regime 1) or 2). The dashed line represents the feasible range of solutions.

7 Linewidth analysis

The optical linewidth of the free-running laser is characterized using the delayed self-heterodyne technique. The experimental configuration, illustrated in Fig. S7a, employs a fiber coupler to split the output of the DFB laser into two paths. One path propagates through an acousto-optic modulator (AOM) applying a 6 MHz frequency shift, while the other through a 30 km single-mode fiber (SMF) delay line. The combined optical signal is detected by a PD and analyzed using an electronic spectrum analyzer (ESA). The power spectrum, offset by the AOM modulation frequency, is presented in Fig. S7b. Since the −3 dB bandwidth of the power spectrum is often larger than the true value due to noise influence near the center frequency, the −20 dB bandwidth is adopted for estimation. This approach leverages the relationship where the −20 dB bandwidth equals $2\sqrt{99}$ times the intrinsic Lorentzian linewidth[4]. The calculated linewidth is 26.4 kHz, corresponding to a coherence length exceeding 11.4 km.

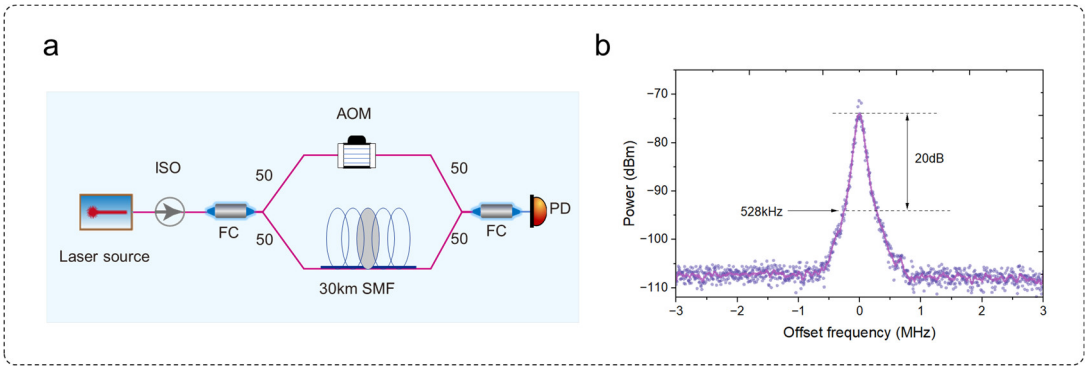

Fig. S7 Linewidth analysis of the employed DFB fiber laser. a Schematic diagram of the delayed self-heterodyne interferometer for coherence length evaluation**.** SMF, single-mode fiber. The isolator is used to block the back-scattering beams, which may induce laser feedback. **b** The frequency-offset spectrum of the detected signal. The linewidth at -20 dB is 528 kHz, corresponding to the linewidth of 26.4 kHz.

8 Fabrication of the swept laser source

The distributed feedback (DFB) fiber laser is selected as the light source, featuring a compact resonator cavity of approximately 50 mm in length. To ensure continuous frequency sweeping, the optical fiber resonator is maintained under constant tensile strain through the application of a preload stress, which is precisely adjusted by monitoring the lasing wavelength. The pre-stressed resonator is then permanently affixed to a PZT using adhesive until complete curing. A 72-mm PZT element is employed to match the resonator length, and it is driven by a symmetric triangular wave signal amplified through a power amplifier.

As illustrated in Fig. S8, the frequency tuning ranges at 10 Hz, 40 Hz, and 100 Hz modulation frequencies exhibit near-identical magnitudes, achieving a 110 GHz sweep bandwidth under 100 Vpp drive voltage. Experimental operations utilize 100 Vpp at 80 Hz.

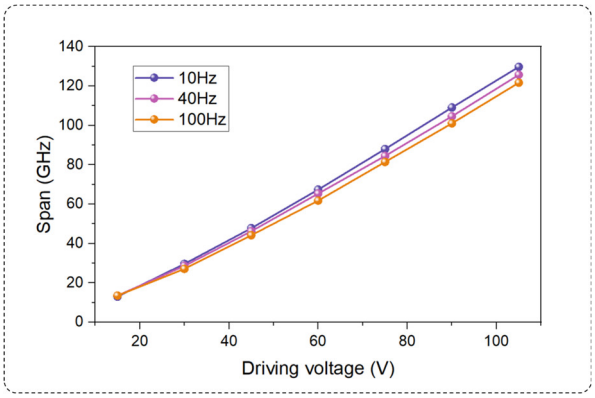

Fig. S8 The modulation bandwidth vs. amplitude of PZT driving signal with various sweep frequencies.

9 Feasibility of resampling in the LFPM system

Current research indicates that the k-sampling calibration method requires satisfaction of the condition[5-7]:

$$|\tau_a^2 \alpha| \ll 1 \tag{S2}$$

where τ_a denotes the auxiliary path delay, $\alpha = dv/dt$ represents the optical frequency sweep rate, v is the optical frequency, and t is time.

Here, we rigorously analyze the validity of this original condition under swept-frequency feedback with increasing feedback strength κ, and derive a revised stability criterion. From Eq. (4) in the main text, the optical frequency evolution in the swept-frequency feedback system is given by[8,9]:

$$\omega(t) = \omega_{c0} + 2\pi\alpha_0 t + \gamma_{ext} \sin\left[\int_{t-\tau_m}^{t} \omega(x)dx\right] \tag{S3}$$

where $\gamma_{ext} = \kappa\gamma_c$, ω_{c0} is the initial laser local oscillation frequency, α_0 is the sweep rate without feedback, and τ_m is the measurement path delay. The following derivation is derived under the condition of weak feedback. When $\gamma_{ext}\tau_m \leq 1$, the system exhibits a single solution (mode-hop-free operation), preserving phase continuity for FMCW ranging. The frequency sweep rate α_0 can be treated as a constant.

Differentiating Eq. (S3) with respect to t yields the actual sweep rate under feedback $\alpha_f(t)$:

$$2\pi\alpha_f(t) = \frac{d\omega(t)}{dt} = 2\pi\alpha_0 + \gamma_{ext} \cos\left[\int_{t-\tau_m}^{t} \omega(x)dx\right][\omega(t) - \omega(t-\tau_m)] \tag{S4}$$

Expanding $\omega(t-\tau_m)$ as a Taylor series around t:

$$\omega(t-\tau_m) = \omega(t) - \frac{d\omega(t)}{dt}\tau_m + \frac{d^2\omega(t)}{2dt^2}\tau_m^2 + \cdots \tag{S5}$$

Assuming the second and higher-order terms are negligible, which means

$$\left|\alpha_f(t)\right| \gg \left|\frac{d\alpha_f(t)}{2dt}\tau_m\right| \tag{S6}$$

Neglecting these terms, we obtain the linearized equation for $\alpha_f(t)$:

$$2\pi\alpha_f(t) = 2\pi\alpha_0 + \gamma_{ext} \cos\left[\int_{t-\tau_m}^{t} \omega(x)dx\right] 2\pi\alpha_f(t)\tau_m \tag{S7}$$

Solving for the actual sweep rate $\alpha_f(t)$ gives:

$$\alpha_f(t) = \frac{\alpha_0}{1 - \gamma_{ext}\tau_m \cos\left[\int_{t-\tau_m}^{t} \omega(x)dx\right]} \tag{S8}$$

Consequently, resampling requires:

$$\max\left(\left|\alpha_f(t)\tau_a^2\right|\right) = \max\left(\left|\frac{\alpha_0}{1 - \gamma_{ext}\tau_m \cos\left[\int_{t-\tau_m}^{t} \omega(x)dx\right]}\tau_a^2\right|\right) \ll 1 \tag{S9}$$

which simplifies to the criterion:

$$\frac{\alpha_0\tau_a^2}{1 - \gamma_{ext}\tau_m} \ll 1 \tag{S10}$$

The following equations are derived to validate the assumption that the second-order quantity is much smaller than that of the first-order.

Refer to Eq. (S6), and take the derivative of $\alpha_f(t)$ with respect to t and ignore higher-order infinitesimals:

$$\frac{d\alpha_f(t)}{2dt}\frac{\tau_m}{\alpha_f(t)} = -\frac{\gamma_{ext}\tau_m^3\alpha_f^2(t)/\alpha_0}{1 + \gamma_{ext}\tau_m^3\alpha_f^2(t)/\alpha_0 \cdot \sin\left[\int_{t-\tau_m}^{t} \omega(x)dx\right]} \sin\left[\int_{t-\tau_m}^{t} \omega(x)dx\right] \tag{S11}$$

For resampling based on auxiliary interference for π-phase interval, the Nyquist theorem requires $\tau_m < 2\tau_a$. When $\alpha_0\tau_a^2/(1 - \gamma_{ext}\tau_m) \ll 1$, it follows that $\alpha_0\tau_m^2/(1 - \gamma_{ext}\tau_m) \ll 1$. The further analysis can be classified into two regimes:

1) For cases of weak feedback**,** where $\gamma_{ext}\tau_m \ll 1$, α_f and α_0 are comparable. Thus, $\gamma_{ext}\tau_m^3\alpha_f^2(t)/\alpha_0 \ll 1$, leading to $|\alpha_f(t)| \gg |\frac{d\alpha_f(t)}{2dt}\tau_m|$.
2) For cases of moderate feedback, where $\gamma_{ext}\tau_m$ is comparable to 1, the condition $\left|\alpha_f(t)\right| \gg \left|\frac{d\alpha_f(t)}{2dt}\tau_m\right|$ must be satisfied as follows:

$$\max\left\{\gamma_{ext}\tau_m^3\alpha_f^2(t)/\alpha_0 \cdot \sin\left[\int_{t-\tau_m}^{t} \omega(x)dx\right]\right\} \approx \max\left[\frac{\tau_m^2\alpha_f^2(t)}{\alpha_0}\right] \ll 1 \tag{S12}$$

Further simplification shows that:

$$\frac{\alpha_0\tau_m^2}{(1 - \gamma_{ext}\tau_m)^2} \ll 1 \tag{S13}$$

In this work, $\kappa\gamma_c$ operates lower than 1 MHz, with the measurement distance on the meter scale. The corresponding round-trip time τ_m and τ_a are on the order of 50 ns. Employing linear displacement-driven PZT frequency tuning achieves sweep rates of around

10 THz/s, thereby meeting the requirements for implementing resampling techniques to suppress frequency-swept nonlinearity.

References

1 Tan, Y. D., Zhang, S. L., Zhang, S., Zhang, Y. Q. & Liu, N. Response of microchip solid-state laser to external frequency-shifted feedback and its applications. *Sci. Rep.* **3**, 2912 (2013).

2 Hao, Y., Song, P., Wang, X. & Pan, Z. A Spectrum Correction Algorithm Based on Beat Signal of FMCW Laser Ranging System. *Sensors* **21**, 5057 (2021).

3 Zhang, S., Zhang, S., Sun, L. & Tan, Y. Spectrum Broadening in Optical Frequency-Shifted Feedback of Microchip Laser. *IEEE Photonic. Tech. L.* **28**, 1593-1596 (2016).

4 Wang, Y. F. *et al.* Frequency-swept feedback interferometry for noncooperative-target ranging with a stand-off distance of several hundred meters. *Photonix* **3**, 21 (2022).

5 Zehao, Y., Cheng, L. & Guodong, L. FMCW LiDAR with an FM nonlinear kernel function for dynamic-distance measurement. *Opt. Express* **30**, 19582-19596 (2022).a

6 Moore, E. D. & McLeod, R. R. Correction of sampling errors due to laser tuning rate fluctuations in swept-wavelength interferometry. *Opt. Express* **16**, 13139-13149 (2008).

7 Barber, Z. W., Babbitt, W. R., Kaylor, B., Reibel, R. R. & Roos, P. A. Accuracy of active chirp linearization for broadband frequency modulated continuous wave ladar. *Appl. Opt.* **49**, 213-219 (2010).

8 Taimre, T. *et al.* Laser feedback interferometry: a tutorial on the self-mixing effect for coherent sensing. *Adv. Opt. Photonics* **7**, 570-631 (2015).

9 Lacot, E., Day, R. & Stoeckel, F. Laser optical feedback tomography. *Opt. Lett.* **24**, 744-746 (1999).